





Technical Note

# Topographic Correction of the SELENE MI Images with the LOLA DEM around Shackleton Crater

Xiaoxue Ke <sup>1,†</sup>, Chao Wang <sup>1,2,3,\*</sup> , Jinhuan Du <sup>1,†</sup>, Yuting Yuan <sup>1,†</sup>, Xiong Xu <sup>1,3</sup>, Yongjiu Feng <sup>1,3</sup>, Huan Xie <sup>1,2,3</sup>, Shijie Liu <sup>1,2,3</sup>  and Xiaohua Tong <sup>1,2,3</sup>

<sup>1</sup> College of Surveying and Geo-Informatics, Tongji University, Shanghai 200092, China

<sup>2</sup> State Key Laboratory of Disaster Reduction in Civil Engineering, Tongji University, Shanghai 200092, China

<sup>3</sup> Shanghai Key Laboratory for Planetary Mapping and Remote Sensing for Deep Space Exploration, Tongji University, Shanghai 200092, China

\* Correspondence: wangchao2019@tongji.edu.cn

† These authors contributed equally to this work.

**Abstract:** Due to the complicated terrain and extreme illumination condition in the lunar south polar region, topography has an impact on the reflectance of the area. This may result in the misinterpretation of the properties of the lunar surface. Therefore, an image obtained across Shackleton Crater by the Multi-band Imager (MI) onboard the first Japanese lunar orbiter SELENE (SELENOlogical and ENgineering Explorer) was utilized to evaluate the topographic effect on the reflectance of the polar region. Three methods—i.e., b correction, C correction, and Minnaert correction—were applied to the MI image to reduce the topographic effect. It was found that the reflectance result of C correction suffers from overcorrection. The topographic effect is enlarged, rather than suppressed, in the reflectance derived with Minnaert correction. Comparatively, b correction is the more appropriate method for the topographic correction of the MI image across the study area. The reflectance of the sunlit slope of the crater wall in the study area decreased by ~60%. The reflectance of the area outside of the crater, with a gentler slope compared to the crater wall, decreased by ~20%. Meanwhile, according to the correlation of the cosine of the local solar incidence angle and the corrected reflectance, the topographic effect was seemingly not completely eliminated in the MI image. However, by analyzing the spectral absorption features of the 1250 nm band, we can attribute this “residual” effect to the different compositions inside and outside of Shackleton Crater, most likely caused by a high concentration of plagioclase. Topographic correction of the MI images over NASA candidate landing regions was also conducted. The results suggest that the topographic effect can contribute significantly to the reflectance of the sunlit slopes, and should not be neglected in the analysis of the reflectance images. This study highlights the topographic impact on the reflectance of the lunar south pole’s surface. In addition, our results also suggest that the compositional differences under various terrains should be considered in the evaluation of the topographic correction of specific regions, such as Shackleton Crater’s inner walls.

**Keywords:** topographic correction; reflectance; lunar south polar region; Shackleton Crater; SELENE MI image; LOLA DEM



**Citation:** Ke, X.; Wang, C.; Du, J.; Yuan, Y.; Xu, X.; Feng, Y.; Xie, H.; Liu, S.; Tong, X. Topographic Correction of the SELENE MI Images with the LOLA DEM around Shackleton Crater. *Remote Sens.* **2022**, *14*, 4739. <https://doi.org/10.3390/rs14194739>

Academic Editor: Roberto Orosei

Received: 7 August 2022

Accepted: 15 September 2022

Published: 22 September 2022

**Publisher’s Note:** MDPI stays neutral with regard to jurisdictional claims in published maps and institutional affiliations.



**Copyright:** © 2022 by the authors. Licensee MDPI, Basel, Switzerland. This article is an open access article distributed under the terms and conditions of the Creative Commons Attribution (CC BY) license (<https://creativecommons.org/licenses/by/4.0/>).

## 1. Introduction

The lunar south pole is a candidate site of high priority for future Moon missions. It features the presence of water ice deposits [1] and other polar volatiles chemicals [2], which are of great importance in understanding the Moon’s evolution and exploiting the lunar resources. NASA’s volatiles investigating polar exploration rover mission intends to land in and traverse the lunar south polar region, exploring the distribution and state of volatiles (e.g., water ice), and evaluating the potential for in situ lunar resource utilization [3]. NASA is also developing a human spaceflight program to land astronauts at the lunar south pole by 2024 [4]. China has planned the Chang’e-7 probe to perform a precise landing in the

Moon's polar regions and a hopping detection in its shadowed areas (from the white paper "China's Space Program: A 2021 Perspective"). China has also released a plan to construct a research station in the lunar south polar region. The potential site of the "Moon Village" proposed by ESA is around the Shackleton Crater at the lunar south pole [5]. The Russian Luna 25 rover will land at the lunar south pole and search for water [6].

The lunar south pole is massively cratered, producing a rugged surface. Therefore, even with the low solar elevation angle ( $\sim 1.5^\circ$ ) induced by the high latitude and small rotational inclination, the sunlit slope can exhibit a high reflectance. This is called the "topographic effect", which emphasizes the fact that the sunlit surface receives more illumination than the shaded slope. For example, it has been reported that the reflectance of the inner wall of Shackleton Crater can be higher than 20% [1,7,8]. Assuming that the high reflectance is due to the presence of water ice deposits, this magnitude of reflectance is equivalent to 20–30 w.t.% water ice. While the high-reflectance regions are mostly in the crater walls, they are highly impacted by the topographic effect. The reported high reflectance around Shackleton Crater [1,7,8] may be due to the sunlit slope, rather than the existence of water ice. Thus, the derived water ice concentration may be misinterpreted. Additionally, although Shackleton Crater is rugged overall, it has small areas those are with flat terrain and long-term illumination conditions [9,10]. Therefore, it is one of the current candidate sites for several future lunar missions based on the consideration of science and engineering. The reflectance of the crater is fundamental both for geological study and mission design (e.g., instrument design and traverse path planning). To investigate the topographic effect on the reflectance, the images captured by the Multi-band Imager (MI)—a high-resolution imaging camera onboard the Japanese Moon orbiter SELENE (SELenological and ENgineering Explorer) [11]—were utilized to conduct topographic correction and evaluation. The MI operates in the visible (VIS) and near-infrared (NIR) wavelengths, covering the characteristic absorption bands of common lunar minerals [11]; it has the capacity to determine the reflectance of the lunar south polar region, with a relatively high resolution and signal-to-noise ratio.

Many methods based on digital elevation models (DEMs) have been developed to reduce the topographic effect. These methods can be divided into three types: empirical, semi-empirical, and physical methods. The *b* correction—an empirical method—corrects the topographic effect based on the empirical relationship between the radiance and the illumination conditions [12]. This relationship can be described by an exponential or linear function. The selection of the function depends on the specific characteristics of the target remote sensing images [12]. The cosine correction—a physical method—is based on Lambert's cosine law; it corrects the topographic effect based on the incidence angle and radiance data [13], and has been further developed as cosine-C correction to compensate for the overcorrection in low-illumination conditions by considering the average solar irradiance [14]. A physical method based on the assumption of non-Lambertian surface, known as Minnaert correction, includes a *k* constant to take the anisotropic scattering into account in order to improve the correction on the shaded slope [15]. C correction is a semi-empirical method, including an empirical correction factor *c* based on the cosine correction to take scatter radiation into account [13]. There are also some methods developed dedicated to the Earth's forest stands based on the sun-canopy-sensor (SCS) geometry, such as SCS correction [16], SCS-C correction [17], and Minnaert-SCS correction [18]. These methods illustrate the fact that trees on the slope are not normal to the surface, but perpendicular to the geoid [16]. For the lunar and Martian surfaces, where no plants are presented, SCS-like methods are not suitable.

Studies have reported that although various topographic correction methods are well-developed, the feasibility of methods for specific remote sensing data needs to be evaluated [19–21]. For MI images, few studies on their topographic correction have been reported. Thus, in order to assess the topographic effect on the reflectance of Shackleton Crater, three typical methods—i.e., *b* correction, C correction, and Minnaert correction—were applied to an MI image taken over the Shackleton Crater's rims. The cor-



rection results were analyzed, and the most suitable method for reducing the topographic effect in MI images was selected. The remainder of this paper is organized as follows: A brief introduction of the data and methods is given in Section 2. In Section 3, the correction results are evaluated. We state our conclusions in Section 4.

## 2. Data and Methods

### 2.1. MI Reflectance and LOLA DEM

The MI is designed to observe the global mineral composition of the lunar surface [11]; it has a spatial resolution of 20 m in VIS and 62 m in NIR, with an orbital altitude of 100 km. The specifications and performance of the MI can be found in [11]. The MI image of the study area is shown in Figure 1a; it contains part of the inner wall of the Shackleton Crater, with a diameter of ~21 km, a depth of ~4.2 km, and an area of ~6000 km<sup>2</sup>. Due to the low solar elevation angle and rugged terrain, most of the crater interiors are permanently shadowed regions (PSRs) [9], where the water ice deposits may be presented and accumulated due to the low temperature [1,22]. Figure 1a shows the 1050 nm reflectance image obtained by the MI on 14th February 2008. The image covers the lunar south pole; it was obtained with a spacecraft altitude of ~106 km, and the solar zenith and azimuth angles were 89.8° and 18.8°, respectively. The emission and phase angles are 1.7° and 88.7°, respectively. From these observation geometries, it can be seen that the sunlight almost comes from the horizon. With such extreme illumination conditions, the lunar surface whose slope is not facing to the Sun is extremely dark; its calibrated reflectance is close to zero. Meanwhile, for the sunlit slope, the reflectance reaches a maximum of 0.167. The contrast of the reflectance between the sunlit and shaded slopes is highly correlated with the topography, as shown in Figure 1.

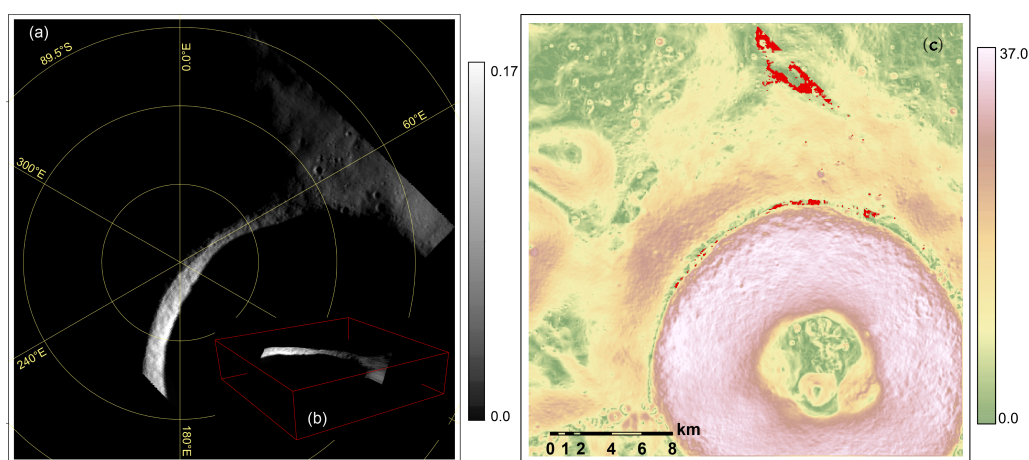


**Figure 1.** (a) The MI 1050 nm reflectance image (MNA\_2B2\_01\_01564S899E0672) of the study area—Shackleton Crater and its surrounding area. (b) The 3D view of the MI image (panel a) with the LOLA DEM. (c) The slope of the lunar south polar region derived from the LOLA DEM, with a spatial resolution of 5 m. The red pixels represent the area with a slope lower than 5°.

The DEM used in this study was obtained by the LOLA (Lunar Orbiter Laser Altimeter) onboard the LRO (Lunar Reconnaissance Orbiter). LOLA is designed to determine the shape of the Moon at high resolution [23]. It has 5 beams to measure the range from the instrument to the lunar surface [23]. The derived LOLA DEM with a spatial resolution of 5 m over the lunar south pole was first resampled to the same resolution as the MI image; then, it was co-registered with the MI image with longitude and latitude, and manually adjusted to achieve better matching for each. The 3D view of the MI image overlaid on the LOLA DEM is shown in Figure 1b, where it can be seen that the variation in reflectance is highly correlated with the topography and the illumination geometries. The slope map derived from the LOLA DEM of the same area shown in Figure 1a is displayed in Figure 1c. Pixels with slope lower than 5° are marked in red. In Figure 1c, only some pixels at the

crater rim are relatively flat around the crater. The average reflectance of these pixels is  $\sim 0.01$  over four NIR bands. It should be noted that this reflectance was measured under a large phase angle, as mentioned above. Since the Moon is airless, little sunlight can be scattered on the shaded slope. The signal-to-noise ratio (SNR) of these slope pixels is very low, resulting in invalid data in this region. Thus, in practice, the pixels for which  $\cos i$  (see Equation (1)) is negative are masked for calculation.

## 2.2. Models for Topographic Correction

Three methods were chosen to reduce the topographic effect in the MI image, i.e., b correction, C correction, and Minnaert correction. Considering the local topography, the local illumination can be described as follows:

$$\cos i = \cos z \cdot \cos S + \sin z \cdot \sin S \cdot \cos(\Phi_s - A) \quad (1)$$

where  $i$  is the local solar incidence angle,  $z$  is the solar zenith angle,  $S$  is the slope angle,  $\Phi_s$  is the solar azimuth angle, and  $A$  is the slope aspect. In b correction, the empirical relationship between  $\cos i$  and observed reflectance can be fitted as follows:

$$L_T = a_1 + b_1 \cdot \cos i \quad (2)$$

where  $L_T$  is the MI reflectance. With  $b_1$ ,  $L_T$  can be corrected as follows:

$$L_H = L_T \cdot \exp[b_1 \cdot (\cos z - \cos i)] \quad (3)$$

where  $L_H$  is the corrected reflectance.

In C correction, the  $L_T$  over the slope is corrected to flat terrain as follows:

$$L_H = L_T \frac{\cos z + c}{\cos i + c} \quad (4)$$

The coefficient  $c$  is obtained as follows:

$$c = a_1 / b_1 \quad (5)$$

where  $a_1$  and  $b_1$  are fitted using Equation (2).

The Minnaert method introduces a constant  $k$  under the assumption of a non-Lambertian surface. The corrected reflectance can be written as follows:

$$L_H = L_T \frac{\cos S}{(\cos S \cdot \cos i)^k} \quad (6)$$

where  $k$  is used to represent the roughness of the surface, which can overcome the over-correction of the methods such as those used in cosine correction, and can be estimated regressively. When  $k = 1$ , the surface is a Lambert reflector [15].

## 2.3. Data Processing

The preprocessing of the MI image and the LOLA DEM is shown in Figure 2. The MI level 1 radiance data were downloaded from the JAXA data archives and transmission system. The MI image was first converted to an image cube file; then it was calibrated in terms of reflectance. After that, the corresponding geometry (i.e., longitude and latitude) and illumination conditions (i.e., solar elevation angle, solar azimuth angle, and emission angle) of each pixel were derived using the USGS Integrated Software for Imagers and Spectrometers [24]. The longitude and latitude were used to georeference and project the images of the reflectance and illumination angles. The 5 m LOLA DEM is were resampled to the resolution of the MI image; then, the DEM and the MI image were matched coarsely based on their geographical positions, and adjusted precisely by selecting the correspondence points. The slope and aspect of the study area were computed with the

DEM. Thus, the spatially consistent MI reflectance, illumination angles, slope, and aspect, were derived and prepared for use in topographic correction.

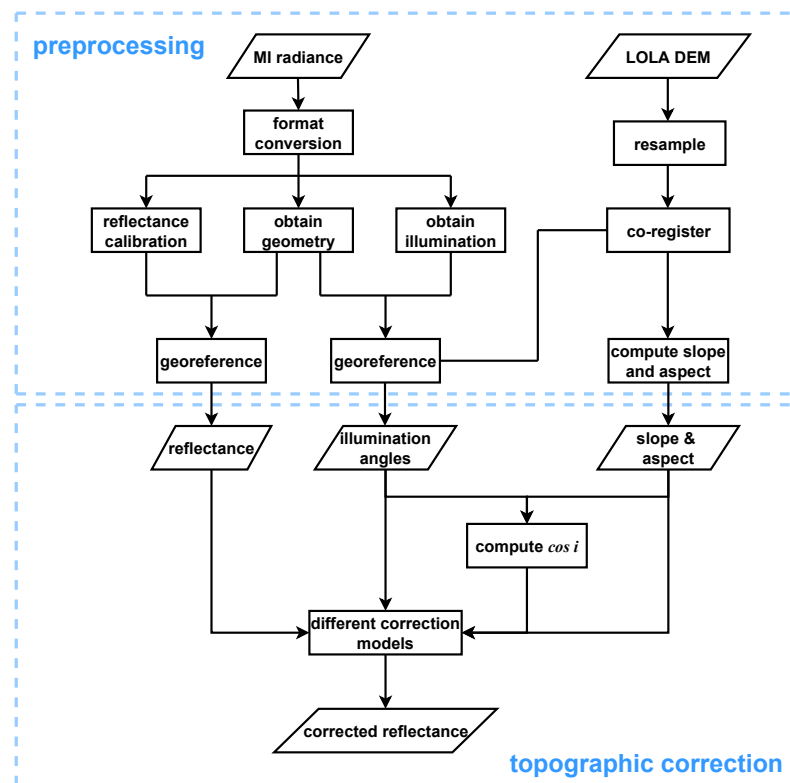
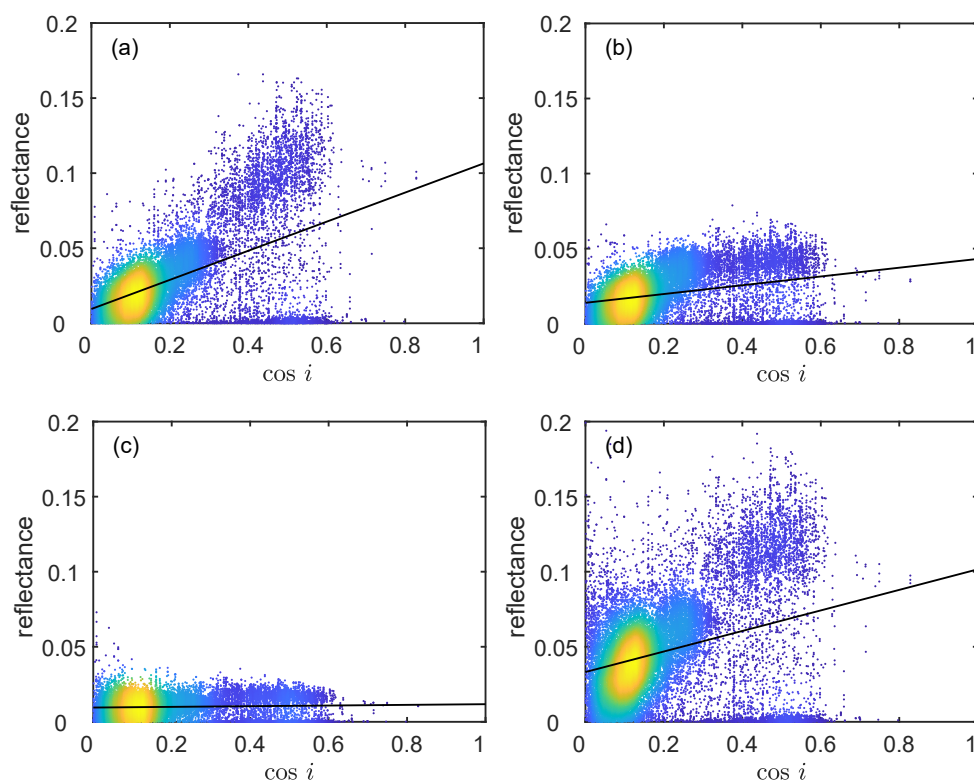


Figure 2. Flow chart of the data processing and topographic correction.

### 3. Results and Discussion

#### 3.1. Correlation of the Reflectance and $\cos i$

The correlation between the reflectance and the cosine of the local solar incidence angle is shown in Figure 3. For the original image, the reflectance and  $\cos i$  are positively correlated. As shown in Figure 3a, the  $\cos i$  is typically lower than 0.3, indicating that more than 85% of the local incidence angles of the valid pixels in the image are larger than  $70^\circ$ . This indicates that even when taking the terrain into account, the surface of the lunar polar region is still observed with large incidence and phase angles. This relatively extreme condition is mainly due to the low solar elevation angle of the study area at a high latitude of the Moon. In Figure 3b–d, the correlations of  $\cos i$  and the corrected reflectance with the three methods are shown. In Figure 3, the scatter points are fitted with linear polynomials. The slopes of the four polynomials are 0.097, 0.029, 0.002, and 0.068, respectively. Compared with the original image, the correlations of the reflectance and  $\cos i$  after b and C correction are significantly reduced, by 70% and 98%, respectively. Additionally, the reflectance corrected with the C method was mainly clustered below 0.04, indicating the darkest pixels among the four plots. The slope of reflectance corrected with the Minnaert method was slightly decreased. The scatter points of the corrected reflectance largely moved upward, as seen in Figure 3d, and their vertical extent was enlarged, meaning that the image was brightened in both sunlit and shadowed slopes, which was not expected after topographic correction.



**Figure 3.** The  $\cos i$  v.s. (a) MI reflectance, and reflectance corrected with (b) b correction, (c) C correction, and (d) Minnaert correction. The color from blue to yellow indicates low to high scatter point density, respectively.

### 3.2. Reflectance Images after Topographic Correction

Figure 4 shows the corrected reflectance images at 1050 nm with the b, C, and Minnaert correction methods. These images are drawn with the same color scale as Figure 1a. Compared with the original MI images, the contrast of the reflectance corrected with the b and C methods is reduced. The reflectance of the sunlit slopes is decreased, and it is close to that of the flat area outside the crater. However, the overall hue of the C-corrected reflectance is dark compared with the other two methods, most likely indicating an overcorrection. The reflectance corrected with the Minnaert method shares similar contrast characteristics with the original image, suggesting that the topographic correction may not have had a positive effect on the MI image. The reflectance of the inner wall of the crater is increased, which was not expected in the topographically corrected images. Additionally, some white spots can be seen in Figure 4c. These artificial pixels are unreasonable; thus, the results suggest that the Minnaert correction is not suitable for the topographic correction of the MI images. Overall, the reflectance image after b correction is relatively acceptable, as shown in Figures 3 and 4. The difference in the reflectance with various local incidence angles is reduced, indicating that the topographic effect has been suppressed. The reflectance image tends to be more homogeneous, and no obvious overcorrection is observed.

The frequencies of the reflectance of the original MI images and those corrected with the three methods are shown in Figure 5. Before the topographic correction, the value of the reflectance extends to a larger range compared with those of the images corrected with the b and C methods, while the image corrected using the Minnaert methods features the brightest reflectance among the four histograms. There are three peaks in the histogram of the original MI image, around 0., 0.02, and 0.1. The first peak, close to zero, reveals the fact that the shadowed area barely receives solar illumination—especially the PSR, such as the inside of Shackleton Crater in the study area. The second peak, around 0.02, represents the area outside the crater, which has a gentler slope compared with the inner wall of the crater,

as shown in Figure 1b. The third peak, with a value of  $\sim 0.1$ , shows the high reflectance of the sunlit inner wall of Shackleton Crater. After topographic correction, the second and third peaks shift leftwards to 0.016 and 0.04, corresponding to a 20% and 60% decrease in reflectance, respectively. The difference in the decrease in reflectance is to be expected, since the inner wall of the crater has a more significant topographic effect due to its deeper slope than the area outside the crater (see Figure 1b). In the histogram of the image corrected with the C methods, only one peak around 0.01 is observed, excluding the one representing the shadowed area.

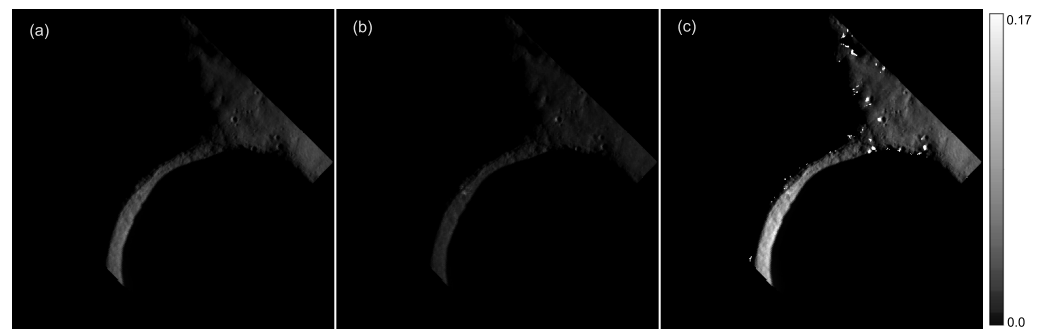


**Figure 4.** Reflectance images at 1050 nm were corrected with (a) b correction, (b) C correction, and (c) Minnaert correction.

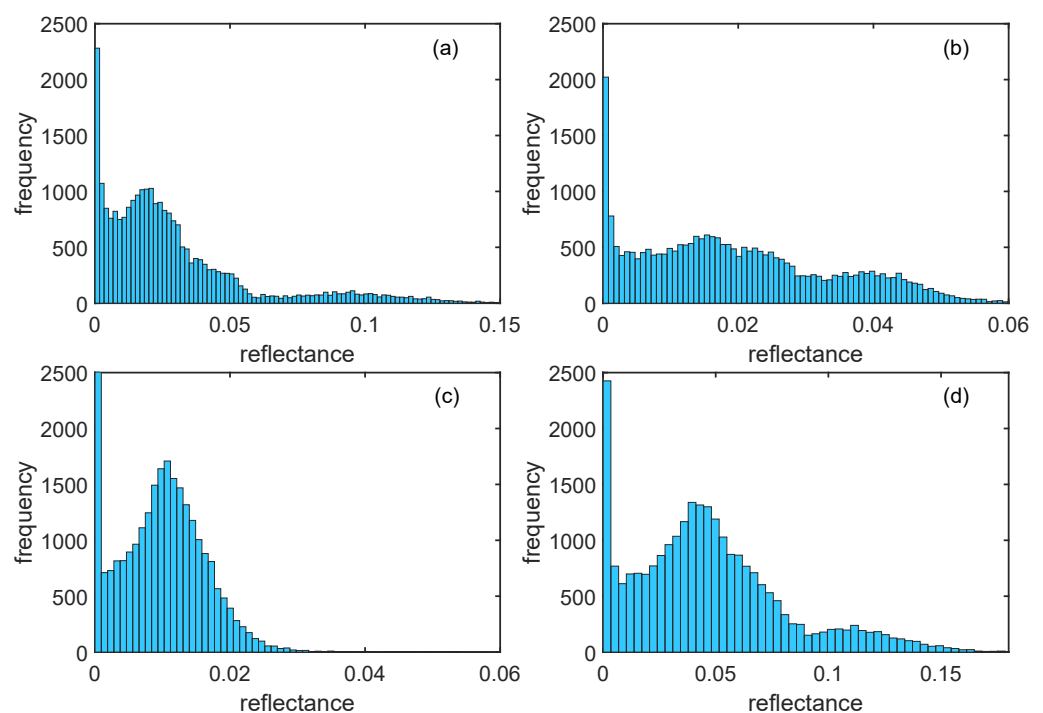


**Figure 5.** Histograms of the (a) original MI image, and the corrected MI images with the (b) b, (c) C, and (d) Minnaert methods. Note that the ranges of the x-axes of the subplots are different.

The mean and the standard deviation of the reflectance before and after topographic correction for the four bands are shown in Table 1. The statistical performance of the four bands is consistent. Both the mean and the standard deviation are decreased after correction. The averaged reflectance for all bands is  $\sim 0.03$  before correction and  $\sim 0.02$  after correction, representing a decrease of 33%. The decrease in reflectance is mainly due to the suppression of the topographic effect of the sunlit slope, which has a significantly high reflectance in the original MI image. The standard deviation of reflectance is  $\sim 0.031$  before correction and 0.016 after correction, representing a reduction of 50%.

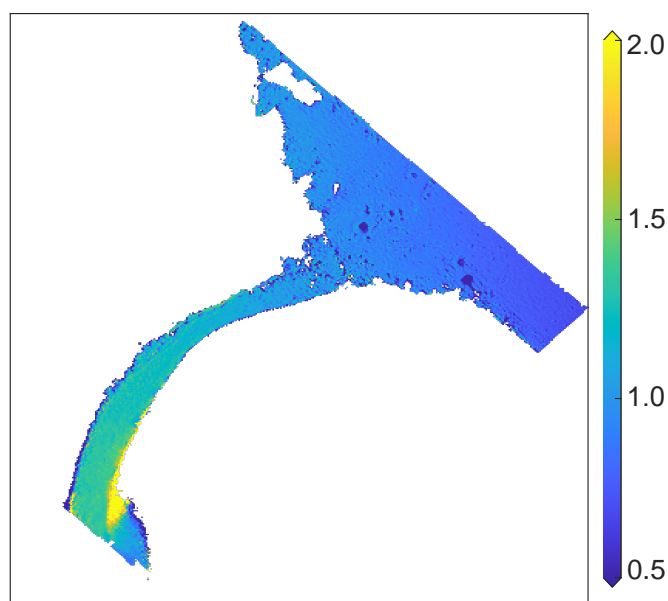


**Table 1.** Mean and standard deviation of the reflectance before and after topographic correction.

MI Band (nm)	Before Correction		After Correction	
	Mean	Std.	Mean	Std.
1000	0.0289	0.0285	0.0197	0.0144
1050	0.0297	0.0294	0.0212	0.0161
1250	0.0320	0.0312	0.0204	0.0156
1550	0.0379	0.0364	0.0241	0.0185

### 3.3. Residual Error Analysis

In Figure 3b, the reflectance corrected with the b method still shows a residual topographic effect, i.e., as the  $\cos i$  increases, the reflectance increases. This feature is particularly apparent with the pixels for which  $\cos i$  is greater than 0.3. These pixels are located on the sunlit inner wall of Shackleton Crater. To unveil the possible reason for this phenomenon, a reflectance ratio image across the study area was produced by dividing the reflectance at 1050 nm by the 1250 nm reflectance image, as shown in Figure 6. It can be seen that outside the crater, the reflectance ratio is mainly lower than 1, while, on the inner wall of the crater, the ratio is greater than those outside the crater—typically greater than 1. This ratio difference implies different spectral absorption characteristics. In the crater, the wall features an absorption around 1250 nm. Among the common minerals on the lunar surface, the plagioclase has a similar spectral feature to this. Moreover, the water ice also has an absorption band around 1300 nm. Water ice and plagioclase have both been found in the walls of Shackleton Crater [1,7,25]. These substances have a higher reflectance at the 1050 nm band than that of the common lunar minerals, such as pyroxene and olivine. This could explain why in Figure 3b the scatter points with the  $\cos i$  greater than  $\sim 0.3$  have a higher reflectance than those with a relatively small  $\cos i$ . This is most likely caused by the different compositions inside and outside the crater, resulting in a higher reflectance of the pixels on the inner wall of the crater. Thus, the “residual topographic effect” is reasonable, and will be retained after topographic correction. Additionally, since water ice in the regolith of the crater wall has not been reported in such a large area, the high reflectance of the crater wall is more likely caused mainly caused by the existence of plagioclase, rather than water ice.

**Figure 6.** Reflectance ratio image of MI 1050/1250 nm across the study area.

### 3.4. Tests on the Candidate Landing Regions

NASA has released the 13 identified candidates landing regions around lunar south polar region for Artemis III; 5 of them—de Gerlache Rims 1 and 2, Connecting Ridge, Connecting Ridge extension, and Peak Near Shackleton—are located at a latitude above  $88^{\circ}\text{S}$ . The DEMs of these five regions are presented in Figure 7. Three MI images covering these regions were selected. Their spatial coverage is plotted with blue rectangles labeled 1–3, as shown in Figure 7. In this section, the results of the topographic correction of these MI images with the b method are presented. The original and corrected images of the 1050 nm band are shown in Figure 8. It can be seen that after correction, the reflectance of the sunlit area of the three images decreased noticeably, and the homogeneity of the surface was improved. Statistically, the mean reflectance of the MI images of de Gerlache Rims 1 and 2, Connecting Ridge and Connecting Ridge extension, and Peak Near Shackleton, is 0.0244, 0.0290, and 0.0281, respectively. After topographic correction, these values decreased to 0.0071, 0.0119, and 0.0122, respectively. This indicates that terrain has a significant impact on the reflectance. Thus, topographic effects should not be neglected in the analysis of the reflectance of the lunar polar region.

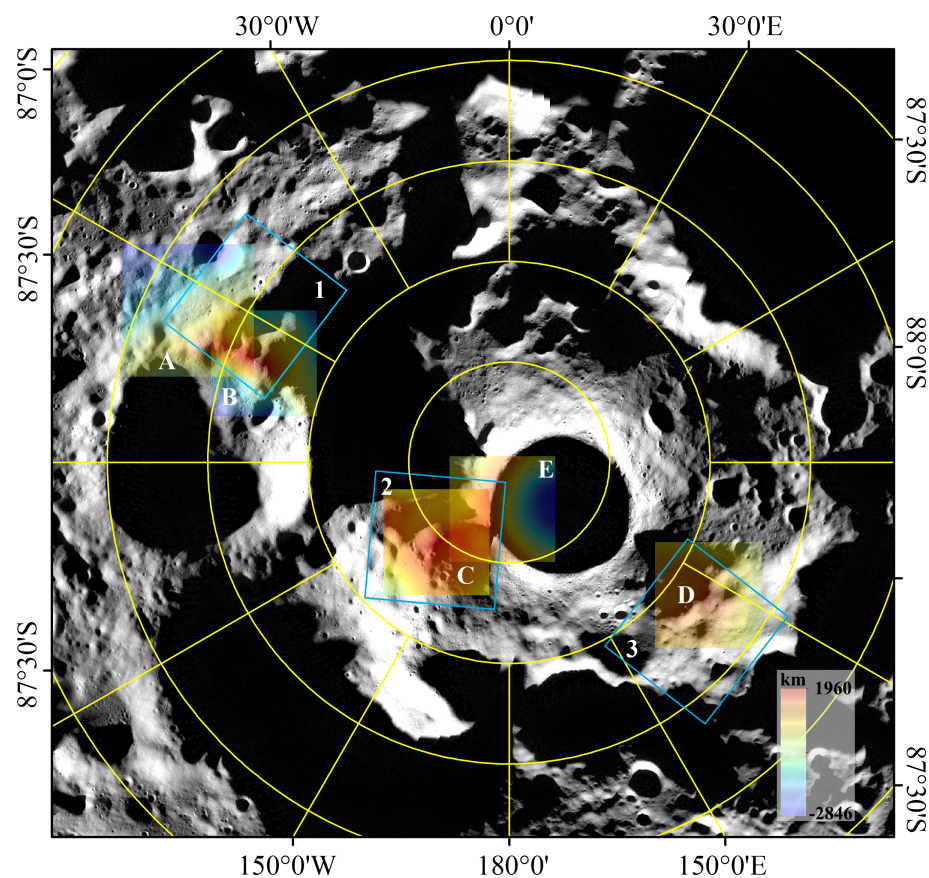


**Figure 7.** The candidate landing regions released by NASA—de Gerlache Rims 1 and 2, Connecting Ridge, Connecting Ridge extension, and Peak Near Shackleton—are labeled A–E, respectively. The locations of the selected three MI images that cover these regions are plotted with blue rectangles labeled 1–3.

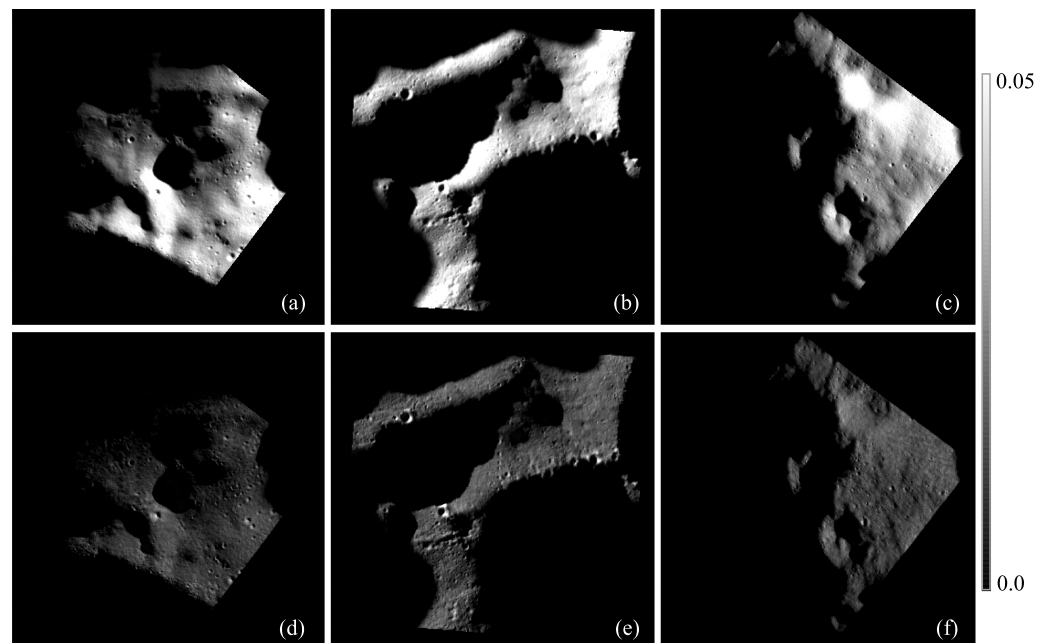


**Figure 8.** The MI images of (a) de Gerlache Rims 1 and 2, (b) Connecting Ridge and Connecting Ridge extension, and (c) Peak Near Shackleton, corresponding to the blue rectangles 1, 2, and 3 in Figure 7, respectively. Panels (d–f) show the images corrected with the b method.

#### 4. Conclusions

The lunar south polar region is an important targeted area for future human Moon missions due to its special geological characteristics. Shackleton Crater in this region is one of the current candidate sites. The reflectance of the lunar surface can be helpful to constrain the composition of the crater, as well as in mission design; however, it may be biased by the topography, leading to a misinterpretation of the properties of the lunar surface. In this paper, a SELENE MI image taken over Shackleton Crater was utilized to investigate and correct the topographic effect. Three methods—i.e., b correction, C correction, and Minnaert correction—were applied to the MI image. By comparing the correlation of local illumination conditions and the corrected reflectance, along with the spatial patterns of the corrected reflectance, we found that although the topographic effect was reduced, overcorrection of the reflectance was observed in the C-corrected image. The topographic effect was not suppressed in the Minnaert-corrected reflectance image; on the other hand, the range of the reflectance was enlarged. Comparatively, the reflectance corrected with the b method yielded more acceptable results. The dependence of the reflectance on the local solar incidence angle was reduced, and the reflectance of the sunlit inner wall of Shackleton Crater decreased by a magnitude of  $\sim 60\%$ , while the reflectance of the area outside the crater (which has a gentler slope) decreased by  $\sim 20\%$ . Moreover, in the image corrected with the b method, a “residual topographic effect” was noticed and discussed. By comparing the spectral absorption around the 1025 nm band, we inferred that the reason for this may be the presence of high concentrations of plagioclase, leading to a higher reflectance of the inner wall than that of the outside of Shackleton Crater in the MI image. In addition, the topographic correction was also conducted on another three MI images, covering five NASA-released candidate landing regions in the south polar region above  $88^\circ\text{S}$ . The corrected results further illustrated the importance of the topographic effect on the MI images in the lunar polar regions. It is worth noting that the reflectance of the study area was corrected to the topography of flat terrain, with a large incidence angle and phase angle in the polar region. If reflectance with standard geometrical conditions is in demand, a photometric correction may be needed to be performed on the images [26].

**Author Contributions:** Conceptualization, C.W., X.K., J.D. and Y.Y.; methodology, C.W., X.K., J.D. and Y.Y.; software, X.K., J.D. and Y.Y.; validation, C.W., X.K., J.D. and Y.Y.; formal analysis, X.K., J.D. and Y.Y.; investigation, X.K., J.D. and Y.Y.; resources, X.X.; data curation, C.W.; writing—original draft preparation, C.W. and Y.Y.; writing—review and editing, C.W., X.X. and Y.F.; visualization, C.W., X.K., J.D. and Y.Y.; supervision, H.X., S.L. and X.T.; project administration, H.X. and X.T.; funding acquisition, C.W. and X.T. All authors have read and agreed to the published version of the manuscript.

**Funding:** This research was funded by the National Natural Science Foundation of China, grant numbers 42171363, 41971299, and 41804166; the Top Discipline Plan of Shanghai Universities-Class I; the Shanghai Municipal Science and Technology Major Project, grant number 2021SHZDZX0100; and the Shanghai Municipal Commission of Science and Technology Project, grant number 19511132101.

**Institutional Review Board Statement:** Not applicable.

**Informed Consent Statement:** Not applicable.

**Data Availability Statement:** The SELENE MI images are available at <https://darts.isas.jaxa.jp/planet/pdap/selene> (accessed on 2 March 2022). The LOLA DEM was downloaded from the NASA PDS Geosciences Node at Washington University at <https://ode.rsl.wustl.edu/moon> (accessed on 24 February 2022).

**Acknowledgments:** The authors would like to thank JAXA for providing the SELENE MI images, as well as NASA for providing the LOLA DEM data.

**Conflicts of Interest:** The authors declare no conflict of interest.

## References

- Li, S.; Lucey, P.G.; Milliken, R.E.; Hayne, P.O.; Fisher, E.; Williams, J.P.; Hurley, D.M.; Elphic, R.C. Direct evidence of surface exposed water ice in the lunar polar regions. *Proc. Natl. Acad. Sci. USA* **2018**, *115*, 8907–8912. [CrossRef] [PubMed]
- Lemelin, M.; Li, S.; Mazarico, E.; Siegler, M.A.; Kring, D.A.; Paige, D.A. Framework for coordinated efforts in the exploration of volatiles in the south polar region of the Moon. *Planet. Sci. J.* **2021**, *2*, 103. [CrossRef]
- Fong, T. NASA—Overview of the 2023 VIPER Lunar Rover Mission—Challenges and Opportunities. In Proceedings of the Australasian Conference on Robotics and Automation, Brisbane, Australia, 8–10 December 2020.
- Smith, M.; Craig, D.; Herrmann, N.; Mahoney, E.; Krezel, J.; McIntyre, N.; Goodliff, K. The Artemis Program: An Overview of NASA’s Activities to Return Humans to the Moon. In Proceedings of the 2020 IEEE Aerospace Conference, Big Sky, MT, USA, 7–14 March 2020; pp. 1–10. [CrossRef]
- Petrov, G.; Inocente, D.; Haney, M.; Katz, N.; Koop, C.; Makaya, A.; Arnhof, M.; Lakk, H.; Cowley, A.; Haignere, C.; et al. Moon Village Reference Masterplan and Habitat Design. In Proceedings of the 49th International Conference on Environmental Systems, Boston, MA, USA, 7–11 July 2019.
- Zelenyi, L.; Mitrofanov, I.; Petrukovich, A.; Khartov, V.; Martynov, M.; Lukianchikov, A. Russian plans for lunar investigations. Stage 1. In Proceedings of the European Planetary Science Congress, Cascais, Portugal, 7–12 December 2014; Volume 9, p. EPSC2014-702.
- Haruyama, J.; Yamamoto, S.; Yokota, Y.; Ohtake, M.; Matsunaga, T. An explanation of bright areas inside Shackleton Crater at the Lunar South Pole other than water-ice deposits. *Geophys. Res. Lett.* **2013**, *40*, 3814–3818. [CrossRef]
- Smith, D.E.; Zuber, M.T.; Neumann, G.A.; Lemoine, F.G.; Mazarico, E.; Torrence, M.H.; McGarry, J.F.; Rowlands, D.D.; Head, J.W.; Duxbury, T.H.; et al. Initial observations from the lunar orbiter laser altimeter (LOLA). *Geophys. Res. Lett.* **2010**, *37*, L18204. [CrossRef]
- Barker, M.K.; Mazarico, E.; Neumann, G.A.; Smith, D.E.; Zuber, M.T.; Head, J.W. Improved LOLA elevation maps for south pole landing sites: Error estimates and their impact on illumination conditions. *Planet Space Sci.* **2021**, *203*, 105119. [CrossRef]
- Mazarico, E.; Neumann, G.; Smith, D.; Zuber, M.; Torrence, M. Illumination conditions of the lunar polar regions using LOLA topography. *Icarus* **2011**, *211*, 1066–1081. [CrossRef]
- Ohtake, M.; Haruyama, J.; Matsunaga, T.; Yokota, Y.; Morota, T.; Honda, C. Performance and scientific objectives of the SELENE (KAGUYA) Multiband Imager. *Earth Planets Space* **2008**, *60*, 257–264. [CrossRef]
- Vincini, M.; Reeder, D.; Frazzi, E. An empirical topographic normalization method for forest TM data. In Proceedings of the IEEE International Geoscience and Remote Sensing Symposium, Toronto, ON, Canada, 24–28 June 2002; Volume 4, pp. 2091–2093. [CrossRef]
- Teillet, P.; Guindon, B.; Goodenough, D. On the slope-aspect correction of multispectral scanner data. *Can. J. Remote. Sens.* **1982**, *8*, 84–106. [CrossRef]
- Civco, D.L. Topographic normalization of landsat thematic mapper digital imagery. *Photogramm. Eng. Remote Sens.* **1989**, *55*, 1303–1309.

15. Smith, J.A.; Lin, T.L.; Ranson, K.J. The Lambertian Assumption and Landsat Data. *Photogramm. Eng. Remote Sens.* **1980**, *46*, 1183–1189.
16. Gu, D.; Gillespie, A. Topographic normalization of Landsat TM images of forest based on subpixel sun–canopy–sensor geometry. *Remote Sens. Environ.* **1998**, *64*, 166–175. [[CrossRef](#)]
17. Soenen, S.A.; Peddle, D.R.; Coburn, C.A. SCS+ C: A modified sun-canopy-sensor topographic correction in forested terrain. *IEEE Trans. Geosci. Remote Sens.* **2005**, *43*, 2148–2159. [[CrossRef](#)]
18. Reeder, D.H. Topographic Correction of Satellite Images: Theory and Application. Ph.D. Thesis, Dartmouth College, Hanover, NH, USA, 2002.
19. Riaño, D.; Chuvieco, E.; Salas, J.; Aguado, I. Assessment of different topographic corrections in Landsat-TM data for mapping vegetation types (2003). *IEEE Trans. Geosci. Remote Sens.* **2003**, *41*, 1056–1061. [[CrossRef](#)]
20. Gao, Y.; Zhang, W. A simple empirical topographic correction method for ETM+ imagery. *Int. J. Remote Sens.* **2009**, *30*, 2259–2275. [[CrossRef](#)]
21. Ma, M.; Wang, C.; Shi, R.; Gao, W. The Research and Assessment of Topographic Registration and Correction of Chang'E-1 IIM Data Based on LRO LOLA DEM Data. *J. Geo-Inf. Sci.* **2015**, *17*, 118–125. [[CrossRef](#)]
22. Paige, D.A.; Siegler, M.A.; Zhang, J.A.; Hayne, P.O.; Foote, E.J.; Bennett, K.A.; Vasavada, A.R.; Greenhagen, B.T.; Schofield, J.T.; McCleese, D.J.; et al. Diviner lunar radiometer observations of cold traps in the Moon's south polar region. *Science* **2010**, *330*, 479–482. [[CrossRef](#)] [[PubMed](#)]
23. Smith, D.E.; Zuber, M.T.; Jackson, G.B.; Cavanaugh, J.F.; Neumann, G.A.; Riris, H.; Sun, X.; Zellar, R.S.; Coltharp, C.; Connelly, J.; et al. The Lunar Orbiter Laser Altimeter investigation on the Lunar Reconnaissance Orbiter mission. *Space Sci. Rev.* **2010**, *150*, 209–241. [[CrossRef](#)]
24. Sides, S.; Becker, T.; Becker, K.; Edmundson, K.; Backer, J.; Wilson, T.; Weller, L.; Humphrey, I.; Berry, K.; Shepherd, M.; et al. The USGS Integrated Software for Imagers and Spectrometers (ISIS 3) instrument support, new capabilities, and releases. In Proceedings of the 48th Annual Lunar and Planetary Science Conference, Houston, TX, USA, 20–24 March 2017; No. 2739.
25. Yamamoto, S.; Nakamura, R.; Matsunaga, T.; Ogawa, Y.; Ishihara, Y.; Morota, T.; Hirata, N.; Ohtake, M.; Hiroi, T.; Yokota, Y.; et al. Massive layer of pure anorthosite on the Moon. *Geophys. Res. Lett.* **2012**, *39*, L13201. [[CrossRef](#)]
26. Yokota, Y.; Matsunaga, T.; Ohtake, M.; Haruyama, J.; Nakamura, R.; Yamamoto, S.; Ogawa, Y.; Morota, T.; Honda, C.; Saiki, K.; et al. Lunar photometric properties at wavelengths 0.5–1.6  $\mu\text{m}$  acquired by SELENE Spectral Profiler and their dependency on local albedo and latitudinal zones. *Icarus* **2011**, *215*, 639–660. [[CrossRef](#)]